



HAL
open science

Modeling of Stress, Distortion, and Hot Tearing

Brian G. Thomas, Michel Bellet

► **To cite this version:**

Brian G. Thomas, Michel Bellet. Modeling of Stress, Distortion, and Hot Tearing. Edited by S. Viswanathan and E. DeGuire. ASM Handbook, Volume 15: Casting, ASM International, pp.Pages 449-461, 2008, ASM Handbooks, 978-0-87170-711-6. hal-00509529

HAL Id: hal-00509529

<https://minesparis-psl.hal.science/hal-00509529>

Submitted on 10 Mar 2011

HAL is a multi-disciplinary open access archive for the deposit and dissemination of scientific research documents, whether they are published or not. The documents may come from teaching and research institutions in France or abroad, or from public or private research centers.

L'archive ouverte pluridisciplinaire **HAL**, est destinée au dépôt et à la diffusion de documents scientifiques de niveau recherche, publiés ou non, émanant des établissements d'enseignement et de recherche français ou étrangers, des laboratoires publics ou privés.

Modeling of Stress, Distortion and Hot Tearing

Brian G. Thomas¹, Michel Bellet²

¹ Department of Mechanical Science & Engineering, University of Illinois (UIUC),
1206 West Green St., Urbana, Illinois, USA, 60801. bgthomas@uiuc.edu

² Ecole des Mines de Paris, Centre de Mise en Forme des Matériaux (CEMEF), UMR CNRS 7635,
BP 207, 06904 Sophia Antipolis, France. michel.bellet@enscm.fr

1 Introduction

Computational modeling of mechanical behavior during solidification is growing in importance. This is because thermal and microstructural simulations alone are insufficient to predict the quality of the final product that is desired by the casting industry. Accurate calculation of displacements, strains, and stresses during the casting process is needed to predict residual stress and distortion, and defects such as the formation of cracks such as hot tears. It also helps in predicting porosity and segregation. As computing power and software tools for computational mechanics advance, it is becoming increasingly possible to perform useful mechanical analysis of castings and these important related behaviors.

The thermomechanical analysis of castings presents a formidable challenge for many reasons:

- Many interacting physical phenomena are involved in stress-strain formation. Stress arises primarily from the mismatch of strains caused by large temperature gradients, and depends on the time- and microstructure- dependent inelastic flow of the material.
- Predicting distortions and residual stresses in cast products requires calculation of the history of the cast product and its environment over huge temperature intervals. This makes the mechanical problem highly non-linear, involving liquid-solid interaction and complex constitutive equations. Even identifying the numerous metallurgical parameters involved in those relations is a daunting task.
- The coupling between the thermal and the mechanical problems is an additional difficulty. This coupling comes from the mechanical interaction between the casting and the mold components, through gap formation or the build-up of contact pressure, modifying locally the heat exchange. This adds some complexity to the non-linear heat transfer resolution.
- Accounting for the mold and its interaction with the casting makes the problem multidomain, usually involving numerous deformable components with coupled interactions.
- Cast parts usually have very complex three-dimensional shapes, which puts great demands on the interface between CAD design and the mechanical solvers, and on computational resources.
- The important length scales range from microns (dendrite arm shapes) to tens of meters (metallurgical length of a continuous caster), with similar huge order-of-magnitude range in time scales.

This chapter summarizes some of the issues and approaches in performing computational analyses of mechanical behavior, distortion and hot-tearing during solidification. The governing equations are presented

first, followed by a brief description of the methods used to solve them, and a few examples of recent applications in shape castings and continuous casting.

2 Governing Equations

The modeling of mechanical behavior requires solution of 1) the equilibrium or momentum equations, relating force and stress; 2) the constitutive equations, relating stress and strain and 3) compatibility equations, relating strain and displacement. This is because the boundary conditions specify either force or displacement at different boundary regions of the domain Ω :

$$\begin{aligned} \mathbf{u} &= \hat{\mathbf{u}} \quad \text{on} \quad \partial\Omega_u \\ \boldsymbol{\sigma}\mathbf{n} &= \hat{\mathbf{T}} \quad \text{on} \quad \partial\Omega_T \end{aligned} \quad (1)$$

where $\hat{\mathbf{u}}$ are prescribed displacements on boundary surface portion $\partial\Omega_u$, and $\hat{\mathbf{T}}$ are boundary surface forces or “tractions” on portion $\partial\Omega_T$. The next sections first present the equilibrium and compatibility equations, and then introduce constitutive equations for the different material states during solidification.

2.1 Equilibrium and compatibility equations

At any time and location in the solidifying material, the conservation of force (steady-state equilibrium) or momentum (transient conditions) can be expressed by:

$$\nabla \cdot \boldsymbol{\sigma} + \rho \mathbf{g} - \rho \frac{d\mathbf{v}}{dt} = 0 \quad (2)$$

where $\boldsymbol{\sigma}$ is the stress tensor, ρ is the density, \mathbf{g} denotes gravity, \mathbf{v} is the velocity field and d/dt denotes the total (particular) time-derivation.. Stress can be further split into the deviatoric stress tensor and the pressure field. The different approaches for simplifying and solving these equations are discussed in Section 2.5.

Once the material has solidified, the internal and gravity forces dominate, so the inertia terms in Eq. (2) can be neglected. Furthermore, the strains which dominate thermo-mechanical behavior during solidification are on the order of only a few percent, or cracks will form. With small gradients of spatial displacement, $\nabla \mathbf{u} = \partial \mathbf{u} / \partial \mathbf{x}$, and the compatibility equations simplify to the following^[1]:

$$\boldsymbol{\varepsilon} = \frac{1}{2} (\nabla \mathbf{u} + (\nabla \mathbf{u})^T) \quad (3)$$

where $\boldsymbol{\varepsilon}$ is the strain tensor and \mathbf{u} is the displacement vector. This small-strain assumption simplifies the analysis considerably. The compatibility equations can also be expressed as a rate formulation, where strains become strain rates, and displacements become velocities. This formulation is more convenient for a transient computation with time integration involving fluid flow and / or large deformation.

In casting analysis, the cast material may be in the liquid, mushy or solid state. Each of these states has different constitutive behavior, as discussed in the next 3 sections.

2.2 Liquid state constitutive models

Metallic alloys generally behave as Newtonian fluids. Including thermal dilatation effects, the constitutive equation can be expressed as follows.

$$\dot{\boldsymbol{\varepsilon}} = \frac{1}{2\mu_l} \mathbf{s} - \frac{1}{3\rho} \frac{d\rho}{dt} \mathbf{I} \quad (4)$$

The strain rate tensor $\dot{\boldsymbol{\varepsilon}}$ is split into two components: a mechanical part, which varies linearly with the deviatoric stress tensor \mathbf{s} , and a thermal part. In this equation, μ_l is the dynamic viscosity of the liquid, ρ is the density, and \mathbf{I} is the identity tensor. Taking the trace of this expression, $\text{tr} \dot{\boldsymbol{\varepsilon}} = \nabla \cdot \mathbf{v}$, the mass conservation equation is recovered:

$$\frac{d\rho}{dt} + \rho \nabla \cdot \mathbf{v} = \frac{\partial \rho}{\partial t} + \nabla \cdot (\rho \mathbf{v}) = 0 \quad (5)$$

In casting processes, the liquid flow may be turbulent, even after mold filling. This may occur because of buoyancy forces or forced convection like in jets coming out of the nozzle outlets in continuous casting processes. The most accurate approach, direct numerical simulation, is generally not feasible for industrial processes, owing to their complex shaped domains and high turbulence. To compute just the large-scale flow features, turbulence models are used, that increase the liquid viscosity according to different models of the small-scale phenomena. These models include the simple "mixing length" models, the two-equation models such as k - ε , and large eddy simulation (LES) models, which have been compared with each other and with measurements of continuous casting.^[2-4]

2.3 Mushy-state constitutive models

Metallic alloys in the mushy state are two-phase liquid-solid media. Their mechanical response depends greatly on the local microstructural evolution, which involves several complex physical phenomena. An accurate description of these phenomena is useful for studying hot tearing or macrosegregation. Knowledge of the liquid flow in the mushy zone is necessary to calculate the transport of chemical species (alloying elements)^[5]. Knowledge of the deformation of the solid phase is important when it affects liquid flow in the mushy zone by "sponge-effects".^[6] In such cases, two-phase models must be used. Starting from microscopic models describing the intrinsic behavior of the liquid phase and the solid phase, spatial averaging procedures must be developed to express the behavior of the compressible solid continuum and of the liquid phase that flows through it^[7-9].

If a detailed description is not really needed, such as in the analysis of residual stresses and distortions, the mushy state can be approximated as a single continuum that behaves as a non-Newtonian (i.e. viscoplastic) fluid, according to the following equations (6) to (8). Thus, the liquid phase is not distinguished from the solid phase, and the individual dendrites and grain boundaries are not resolved.

$$\dot{\boldsymbol{\varepsilon}} = \dot{\boldsymbol{\varepsilon}}^{vp} + \dot{\boldsymbol{\varepsilon}}^{th} \quad (6)$$

$$\dot{\boldsymbol{\varepsilon}}^{vp} = \frac{3}{2K} (\dot{\boldsymbol{\varepsilon}}_{eq})^{1-m} \mathbf{s} \quad (7)$$

$$\dot{\boldsymbol{\varepsilon}}^{th} = -\frac{1}{3\rho} \frac{d\rho}{dt} \mathbf{I} \quad (8)$$

K is the viscoplastic consistency and m the strain rate sensitivity. Denoting $\sigma_{eq} = \sqrt{\frac{3}{2} s_{ij} s_{ij}}$ the von Mises equivalent stress scalar, and $\dot{\epsilon}_{eq} = \sqrt{\frac{2}{3} \dot{\epsilon}_{ij}^{vp} \dot{\epsilon}_{ij}^{vp}}$ the von Mises equivalent strain rate scalar, Eq. (7) yields the well known power law: $\sigma_{eq} = K(\dot{\epsilon}_{eq})^m$. Note that the preceding Newtonian liquid model is actually a particular case of this non-Newtonian one: Eq. (4) can be derived from Eq. (6), (7) and (8) taking $m = 1$ and $K = 3\mu_l$. The solidification shrinkage is included in Eq. (8): writing $\rho = g_s \rho_s + g_l \rho_L$ in the solidification interval, (ρ_s, ρ_L densities at the solidus and liquidus temperatures respectively, g_s, g_l volume fractions of solid and liquid respectively), the thermal strain rate is defined as follows:

$$\text{tr} \dot{\epsilon}^{th} = -\frac{1}{\rho} \frac{d\rho}{dt} = -\frac{1}{\rho} (\rho_s - \rho_L) \frac{dg_s}{dt} \approx \frac{\rho_L - \rho_s}{\rho_L} \frac{dg_s}{dt} \quad (9)$$

2.4 Solid-state constitutive models

In the solid state, metallic alloys can be modeled either as elastic-plastic or elastic-viscoplastic materials. In the latter class of models, one of the simpler is expressed as follows, but it should be mentioned that a lot of models of different complexity can be found in the literature.^[10, 11]

$$\dot{\epsilon} = \dot{\epsilon}^{el} + \dot{\epsilon}^{in} + \dot{\epsilon}^{th} \quad (10)$$

$$\dot{\epsilon}^{el} = \frac{1+\nu}{E} \dot{\sigma} - \frac{\nu}{E} \text{tr}(\dot{\sigma}) \mathbf{I} + \dot{T} \frac{\partial}{\partial T} \left(\frac{1+\nu}{E} \right) \sigma - \dot{T} \frac{\partial}{\partial T} \left(\frac{\nu}{E} \right) \text{tr}(\sigma) \mathbf{I} \quad (11)$$

$$\dot{\epsilon}^{in} = \frac{3}{2\sigma_{eq}} \left\langle \frac{\sigma_{eq} - \sigma_0}{K} \right\rangle^{1/m} \mathbf{s} \quad (12)$$

$$\dot{\epsilon}^{th} = -\frac{1}{3\rho} \frac{d\rho}{dt} \mathbf{I} \quad (13)$$

The strain rate tensor $\dot{\epsilon}$ is split into an elastic component, an inelastic (non reversible) component, and a thermal component. Equation (11) is the hypoelastic Hooke's law, where E is Young's modulus, ν the Poisson's coefficient, and $\dot{\sigma}$ a time derivative of the stress tensor σ . Equation (12) gives the relation between the inelastic strain rate tensor $\dot{\epsilon}^{in}$ and the stress deviator, \mathbf{s} , in which σ_0 denotes the scalar static yield stress, below which no inelastic deformation occurs (the expression between brackets is reduced to zero when negative). In these equations, the temperature dependency of all the involved variables should be considered. The effect of strain hardening may appear in such a model by the increase of both the static yield stress σ_0 and the plastic consistency K with the accumulated inelastic strain ϵ_{eq} , or with another state variable that is representative of the material structure. The corresponding scalar equation relating stress and inelastic strain rate von Mises invariants is:

$$\sigma_{eq} = \sigma_0 + K(\dot{\epsilon}_{eq})^m \quad (14)$$

Inserting this into Eq. (12) simplifies it to:

$$\dot{\epsilon}^{in} = \frac{3\dot{\epsilon}_{eq}}{2\sigma_{eq}} \mathbf{s}, \text{ or, in incremental form, } d\epsilon^{in} = \frac{3d\epsilon_{eq}}{2\sigma_{eq}} \mathbf{s} \quad (15)$$

Although metallic alloys show a significant strain rate sensitivity at high temperature, they are often modelled in the literature using elastic-plastic models, neglecting this important effect. In this case, Eq. (15) still holds, but the flow stress is independent of the strain rate. It may depend on the accumulated plastic strain because of strain hardening.

2.5 Implementation Issues

One of the major difficulties in the thermomechanical analysis of casting processes is the concurrent presence of liquid, mushy and solid regions which move with time as solidification progresses. Several different strategies have been developed, according to the process and model objectives.

- A first strategy consists in extracting the solidified regions of the casting domain based on the thermal analysis results. Then, a small-strain thermo-mechanical analysis is carried out on just this solid subdomain, using a standard solid-state constitutive model. Beside difficulties with the extraction process, especially when the solidified regions have complex unconnected shapes, this method may have numerical problems with the application of the liquid hydrostatic pressure onto the new internal boundary of the solidified region. However, this simple strategy is very convenient for many practical problems, especially when the solidification front is stationary, such as the primary cooling of continuous casting of aluminum,^[12] and steel^[13, 14]. For transient problems, such as the prediction of residual stress and shape (butt-curl) during startup of the aluminum DC continuous casting process, the domain can be extended in time by adding layers.^[12]
- A second strategy considers the entire casting, including the mushy and liquid regions. The liquid, mushy and solid regions are modeled as a continuum by adopting the constitutive equations for the solid phase (Section 2.4) for all regions by adjusting material parameters such as K , m , E , ν , σ_0 , and ρ according to temperature. For example, liquid can be treated by setting the strains to zero when the temperature is above the solidus temperature. This ensures that stress development in the liquid phase is suppressed. In the equilibrium equation, Eq. 2, acceleration terms are neglected, and a small-strain analysis can be performed. The primary unknowns are the displacements, or displacement increments. This popular approach can be used with structural finite element codes, such as MARC^[15] or ABAQUS^[16] and with commercial solidification codes or special-purpose software, such as ALSIM^[17] / ALSPEN,^[18] CASTS,^[19] CON2D,^[20, 21] MagmaSoft,^[22] and Procast.^[23, 24] It has been applied successfully to simulate deformation and residual stress in shape castings,^[25, 26] DC casting of aluminum,^[12, 17, 18, 27-29] and continuous casting of steel^[20, 30] Despite its efficiency, this approach may suffer from several drawbacks. First, it cannot properly account for fluid flow and the volumetric shrinkage that affects flow in the liquid pool, fluid feeding into the mushy zone, and primary shrinkage depressions that affect casting shape. In addition, incompressibility of the metal in the liquid state is accounted for by increasing Poisson's ratio close to 0.5, which sometimes makes the solution prone to numerical instability.^[31, 32]
- A third strategy has been recently developed, which addresses the above issues. It still simulates the entire casting, but treats the mass and momentum equations of the liquid and mushy regions with a mixed velocity-pressure formulation. The primary unknowns are the velocity (time derivative of displacement) and pressure fields, which makes it easier to impose the incompressibility constraint (see section 4). Indeed, the velocity-pressure formulation is also applied to the equilibrium of the solid regions, in order to provide a single continuum framework for the global numerical solution. This strategy has been implemented into codes dedicated to casting analysis such as THERCAST,^[30, 33, 34] and VULCAN^[35]. If stress prediction is not important so that elastic strains can be ignored,

then this formulation simplifies to a standard fluid flow analysis, which is useful in the prediction of bulging and shape in large-strain processes.

2.6 Example of Solid-State Constitutive Equations

Material property data are needed for the specific alloy being modeled and in a form suitable for the constitutive equations just discussed. This presents a significant challenge for quantitative mechanical analysis, because measurements are not presented in this form, and only rarely supply enough information on the conditions to allow transformation to an alternate form. As an example, the following elastic-viscoplastic constitutive equation was developed for the austenite phase of steel^[36] by fitting constant strain-rate tensile tests^[37, 38] and constant-load creep tests^[39] to the form required in Eqs. (10)-(13).

$$\dot{\epsilon}_{eq} = f_{\%C} \langle \sigma_{eq} - \sigma_0 \rangle^{1/m} \exp\left(-\frac{4.465 \times 10^4}{T}\right)$$

where

$$f_{\%C} = 4.655 \times 10^4 + 7.14 \times 10(\%C) + 1.2 \times 10^4 (\%C)^2 \quad (16)$$

$$\sigma_0 = (130.5 - 5.128 \times 10^{-3} T) \epsilon_{eq}^{f_2}$$

$$f_2 = -0.6289 + 1.114 \times 10^{-3} T$$

$$1/m = 8.132 - 1.54 \times 10^{-3} T$$

with T [K], σ_{eq} , σ_0 [MPa]

This equation, and a similar one for delta-ferrite, have been implemented into the finite-element codes CON2D^[20] and THERCAST^[40] and applied to investigate several problems involving mechanical behavior during continuous casting.

Elastic modulus is a crucial property that decreases with increasing temperature. It is difficult to measure at the high temperatures important to casting, owing to the susceptibility of the material to creep and thermal strain during a standard tensile test, which results in excessively low values. Higher values are obtained from high-strain-rate tests, such as ultrasonic measurements.^[41] Elastic modulus measurements in steels near the solidus temperature range from ~1 GPa^[42] to 44 GPa.^[43] with typical modulus values ~10 GPa near the solidus.^[44-46]

The density needed to compute thermal strain in Eqs. (4), (8) or (13) can be found from a weighted average of the values of the different solid and liquid phases, based on the local phase fractions. For the example of plain low carbon steel, the following equations were compiled^[20] based on solid data for ferrite (α), austenite (γ), and delta (δ)^[47, 48] and liquid (l) measurements.^[49]

$$\rho(kg/m^3) = \rho_{\alpha} f_{\alpha} + \rho_{\gamma} f_{\gamma} + \rho_{\delta} f_{\delta} + \rho_l f_l$$

$$\rho_{\alpha} = 7881 - 0.324T(^{\circ}C) - 3 \times 10^{-5} T(^{\circ}C)^2$$

$$\rho_{\gamma} = \frac{100[8106 - 0.51T(^{\circ}C)]}{[100 - (\%C)][1 + 0.008(\%C)]^3} \quad (17)$$

$$\rho_{\delta} = \frac{100[8011 - 0.47T(^{\circ}C)]}{[100 - (\%C)][1 + 0.013(\%C)]^3}$$

$$\rho_l = 7100 - 73(\%C) - [0.8 - 0.09(\%C)][T(^{\circ}C) - 1550]$$

Specialized experiments to measure mechanical properties for use in computational models will be an important trend for future research in this field.

3 Thermomechanical coupling

Coupling between the thermal and mechanical analyses arises from several sources. First, regarding the mechanical problem, besides the strain rate due to thermal expansion and solidification shrinkage, the material parameters of the preceding constitutive equations strongly depend on temperature and phase fractions, as shown in the previous section. Second, in the heat transfer problem, the thermal exchange between the casting and the mold strongly depends on local conditions such as the contact pressure or the presence of a gap between them (as a result of thermal expansion and solidification shrinkage). This is illustrated in Figure 1 and discussed hereunder.

3.1.1 Air gap formation: conductive-radiative modeling

In the presence of a gap between the casting and the mold, resulting from their relative deformation, the heat transfer results from concurrent conduction through the gas within the gap and from radiation. The exchanged thermal flux, q_{gap} , can then be written:

$$q_{gap} = \frac{k_{gas}}{g}(T_c - T_m) + \frac{\sigma(T_c^4 - T_m^4)}{\frac{1}{\epsilon_c} + \frac{1}{\epsilon_m} - 1} \quad (18)$$

with $k_{gas}(T)$ the thermal conductivity of the gas, g the gap thickness, T_c and T_m the local surface temperature of the casting and mold, respectively, ϵ_c and ϵ_m their gray-body emissivities, σ the Stefan-Boltzmann constant. It is to be noted that the conductive part of the flux can be written in more detail to take into account the presence of coating layers on the mold surface: conduction through a medium of thickness g_{coat} , of conductivity $k_{coat}(T)$. It can be seen that the first term tends to infinity as the gap thickness tends to zero: this expresses a perfect contact condition, T_c and T_m tending towards a unique interface temperature. The reality is somewhat different, showing always non perfect contact conditions. Therefore, the conductive heat exchange coefficient $h_{cond} = k_{gas}/g$ should be limited by a finite value h_0 , corresponding to the “no-gap” situation, and depends on the roughness of the casting surface. Specific examples of these gap heat transfer laws are provided elsewhere for continuous casting with oil lubrication,^[13] and mold flux.^[50]

3.1.2 Effective contact : heat transfer as a function of contact pressure

With effective contact, the conductive heat flux increases with the contact pressure according to a power law.^[51] Still denoting h_0 as the heat exchange coefficient corresponding to no gap and no contact pressure, the interfacial heat flux is:

$$q_{contact} = (h_0 + Ap_c^B)(T_c - T_m) \quad (19)$$

with p_c the contact pressure, A and B two parameters which depend on the materials, the presence of coating or lubricating agent, the surface roughness, and the temperature. The parameters and possibly the laws governing their evolution need to be determined experimentally.

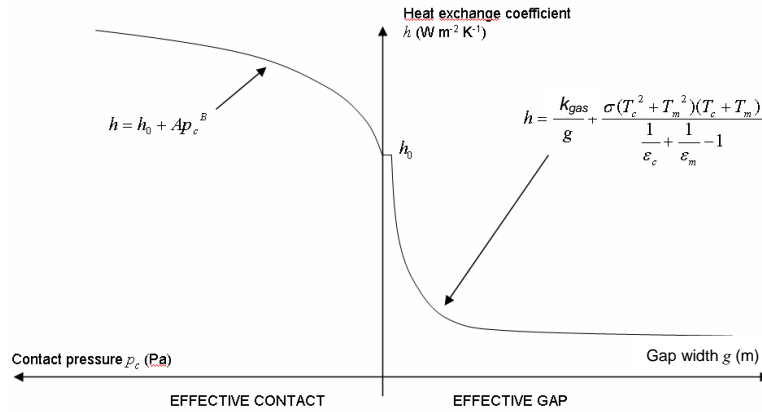


Figure 1. Modeling of the local heat transfer coefficient in the gap and effective contact situations.

4 Numerical solution

The thermal-mechanical modeling equations just presented must be solved numerically, owing to the complex shape of the casting process domain, and the highly nonlinear material properties. The calculation depends greatly on the numerical resolution of time and space. Although finite-difference approaches are popular for heat transfer, solidification, and fluid flow analyses, the finite element formulation is usually preferred for the mechanical analysis, owing to its historical advantages with unstructured meshes and accurate implicit solution of the resulting simultaneous algebraic equations. The latter are discussed below.

4.1 Finite element formulation and numerical implementation

In the framework of the small strain approach presented above (section 2.5), having displacements for primitive unknowns, the weak form of the equilibrium equation, Eq. (2), neglecting inertia terms, is written as:

$$\forall \mathbf{u}^* \int_{\Omega} \boldsymbol{\sigma} : d\boldsymbol{\varepsilon}(\mathbf{u}^*) dV - \int_{\partial\Omega} \mathbf{T} \cdot \mathbf{u}^* dS - \int_{\Omega} \rho \mathbf{g} \cdot \mathbf{u}^* dV = 0 \quad (20)$$

where \mathbf{T} is the external stress vector. The vector test-functions \mathbf{u}^* can be seen as virtual displacements in a statement of virtual work.

If the third strategy described in section 2.5 is adopted, with velocity and pressure as primary unknown variables, the weak form of the momentum equation (Eq. (2)) is written as^[52]:

$$\left\{ \begin{array}{l} \forall \mathbf{v}^* \int_{\Omega} \mathbf{s} : \dot{\boldsymbol{\varepsilon}}(\mathbf{v}^*) dV - \int_{\Omega} p \nabla \cdot \mathbf{v}^* dV - \int_{\partial\Omega} \mathbf{T} \cdot \mathbf{v}^* dS - \int_{\Omega} \rho \mathbf{g} \cdot \mathbf{v}^* dV + \int_{\Omega} \rho \frac{d\mathbf{v}}{dt} \cdot \mathbf{v}^* dV = 0 \\ \forall p^* \int_{\Omega} p^* \text{tr} \dot{\boldsymbol{\varepsilon}}^{in} dV = 0 \end{array} \right. \quad (21)$$

The first equation, contains vector test-functions \mathbf{v}^* , which can be seen as virtual velocities in a statement of virtual power. Unlike Eq. (20), the pressure p is a primary variable, and only the deviatoric part of the constitutive equations is involved (to determine the stress deviator \mathbf{s}). This is why the second equation is needed, which consists of a weak form of the incompressibility of inelastic deformations.

Equations (20) and (21) are spatially discretized using the standard finite-element method, as explained in detail in many references.^[52] Combined with time discretization using finite differences, this leads to a set of non-linear equations to be solved at each time increment. In the context of the displacement strategy, Eq. (20), this leads to:

$$\mathbf{R}(\mathbf{U}) = 0 \quad (22)$$

where \mathbf{R} is the vector of the nodal equilibrium residues (number of components: 3 x number of nodes, in dimension 3), and \mathbf{U} is the vector of nodal incremental displacements (same size).

Adopting the velocity-pressure strategy, Eq. (21), leads to a set of non-linear equations:

$$\mathbf{R}'(\mathbf{V}, \mathbf{P}) = 0 \quad (23)$$

where \mathbf{R}' is the vector of the nodal residues (number of components: 4 x number of nodes, in dimension 3), \mathbf{V} is the vector of nodal velocities (size: 3 x number of nodes) and \mathbf{P} is the vector of nodal pressures (size: number of nodes).

The global finite-element systems (22) or (23) are usually solved using a full or modified Newton-Raphson method,^[31, , 2004 #3715] which iterates to minimize the norm of the residue vectors \mathbf{R} or \mathbf{R}' . Alternatively, explicit methods may be employed at this global level.

At the local (finite element) level, an algorithm is also required to integrate the constitutive equations, when they depend on strain-rate or strain. When the constitutive equations are highly non-linear, an implicit algorithm is useful to perform time integration at each Gauss point in order to provide better estimates of inelastic strain at the local level.^[53-55]

4.2 Boundary conditions: modeling of contact conditions. Multidomain approaches

At the interface between the solidifying material and the mold, a contact condition is required to prevent penetration of the shell into the mold, while allowing shrinkage of the shell away from the mold to create an interfacial gap:

:

$$\begin{cases} \boldsymbol{\sigma}\mathbf{n} \cdot \mathbf{n} \leq 0 \\ g \geq 0 \\ (\boldsymbol{\sigma}\mathbf{n} \cdot \mathbf{n}) g = 0 \end{cases} \quad (24)$$

where g is the local interface gap width (positive when air gap exists effectively, as in section 3.1.1) and \mathbf{n} is the local outward unit normal to the part. Eq. (24) can be satisfied with a penalty condition, which consists in applying a normal stress vector \mathbf{T} proportional to the penetration depth (if any) via a penalty constant χ_p :

$$\mathbf{T} = \boldsymbol{\sigma}\mathbf{n} = -\chi_p \langle -g \rangle \mathbf{n} \quad (25)$$

Here again, the brackets denote the positive part: a repulsive stress is applied only if g is negative (penetration). Different methods of local adaptation of the penalty coefficient χ_p have been developed, including the augmented Lagrangian method.^[56] More complex and computationally expensive methods, such as the use of Lagrange multipliers may also be used.^[57]

The possible tangential friction effects between part and mold can be taken into account by a friction law, such as a Coulomb model for instance. In this case, the previous stress vector has a tangential component, \mathbf{T}_τ , given by:

$$\mathbf{T}_\tau = -\mu_f p_c \frac{1}{\|\mathbf{v} - \mathbf{v}_{mold}\|} (\mathbf{v} - \mathbf{v}_{mold}) \quad (26)$$

where $p_c = -\sigma_n = -\boldsymbol{\sigma}\mathbf{n} \cdot \mathbf{n}$ is the contact pressure, and μ_f the friction coefficient.

The previous approach can be extended to the multidomain context in order to account for the deformation of mold components. The local stress vectors calculated by Eq. (25) can be applied onto the surface of the mold, contributing then to its deformation. For most casting processes, the mechanical interaction between the cast product and the mold is sufficiently slow (i.e. its characteristic time remains significant with respect to the process time) to permit a staggered scheme within each time increment: the mechanical problem is successively solved in the cast product and in the different mold components. A global updating of the different configurations is then performed at the end of the time increment. This simple approach gives access to a prediction of the local air gap size g , or alternatively of the local contact pressure p_c , that are used in the expressions of the heat transfer coefficient, according to Eqs. (18) and (19).^[58]

4.3 Treatment of the regions in the solid, mushy and liquid states

4.3.1 Solidified regions: Lagrangian formulation

In casting processes, the solidified regions generally encounter small deformations. It is thus natural to embed the finite element domain into the material, with each node of the computational grid corresponding with the same solid particle during its displacement. The boundary of the mesh corresponds then to the surface of the casting. This method, called Lagrangian formulation, provides the best accuracy when computing the gap forming between the solidified material and the mold. It is also the more reliable and convenient method for time integration of highly non-linear constitutive equations, such as elastic-(visco)-plastic laws presented in section 2.4.

4.3.2 Mushy and liquid regions: ALE modeling

When the mushy and liquid regions are modeled in the same domain as the solid (cf. discussion in section 2.5), they are often subjected to large displacements and strains arising from solidification shrinkage, buoyancy, or forced convection. Similar difficulties are generated in casting processes such as squeeze casting, where the entire domain is highly deformed. In these cases, a Lagrangian formulation would demand frequent remeshings in order to avoid mesh degeneracy, which is both computationally costly, and detrimental to the accuracy of the modeling. It is then preferable to use a so-called arbitrary Lagrangian Eulerian formulation (ALE). In an Eulerian formulation, material moves through the computational grid, which remains stationary in the “laboratory” frame of reference. In the ALE formulation, the updating of the mesh is partially independent of the velocity of the material particles in order to maintain the quality of the computational grid. Several methods can be used, including the popular “barycentering” technique which keeps each node at the geometrical centroid of a set of its neighbors. This method involves significant extra complexity to account for the advection of material through the domain, and the state variables such as temperature and inelastic strain must be updated according to the relative velocity between the mesh and the particles. In doing this, some surface constraints must be enforced in order to ensure mass conservation, expressing that the fluxes of mesh velocity and of fluid particle velocity through the surface of the mesh should remain identical. A review on the ALE method in solidification modeling is available, together with some details on its application.^[33]

4.4 Thermomechanical coupling

Because of the interdependency of the thermal and mechanical analyses, as presented in section 3, their coupling should be taken into account all during the cooling process. In practice, the cooling time is decomposed into time increments, each increment requiring the solution of two problems: the energy conservation and the momentum conservation. With the highly nonlinear elastic-visco-plastic constitutive equations typical of solidifying metals, the incremental steps required for the mechanical analysis to converge are generally much smaller than those for the thermal analysis. Thus, these two analyses are generally performed in succession and only once per time increment. However, in the case of very rapid cooling, these solutions might be preferably performed together (including thermal and mechanical unknowns in a single set of non-linear equations), or else separate but iteratively until convergence at each time increment, otherwise the time step has to be dramatically reduced.

5 Model Validation

Model validation with both analytical solutions and experiments is a crucial step in any computational analysis and thermo-mechanical modeling is no exception. Weiner and Boley^[59] derived an analytical solution for unidirectional solidification of an unconstrained plate with a unique solidification temperature, an elastic-perfectly-plastic constitutive law and constant properties. The plate is subjected to sudden surface quench from a uniform initial temperature to a constant mold temperature.

This benchmark problem is ideal for estimating the discretization errors of computational thermal-stress models, as it can be solved with a simple mesh consisting of one row elements, as shown in Figure 2. Numerical predictions should match with acceptable precision using the same element type and mesh refinement planned for the real problem. For example, the solidification stress analysis code, CON2D^[20] and the commercial code ABAQUS were applied for typical conditions of steel casting.^[21]

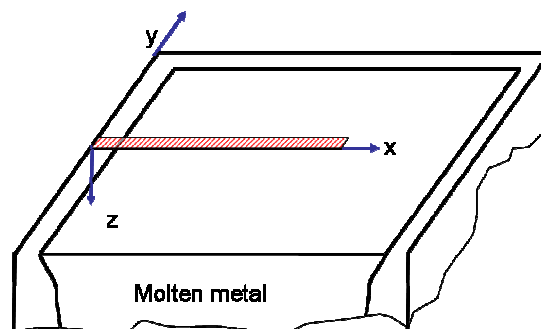


Figure 2. One-dimensional slice-domain for modeling solidifying plate.

Figure 3 and Figure 4 compare the temperature and stress profiles in the plate at two times. The temperature profile through the solidifying shell is almost linear. Because the interior cools relative to the fixed surface temperature, its shrinkage generates internal tensile stress, which induces compressive stress at the surface. With no applied external pressure, the average stress through the thickness must naturally equal zero, and stress must decrease to zero in the liquid. Stresses and strains in both transverse directions are equal for this symmetrical problem. The close agreement demonstrates that both computational models are numerically consistent and have an acceptable mesh resolution. Comparison with experimental measurements is also required, to validate that the modeling assumptions and input data are reasonable.

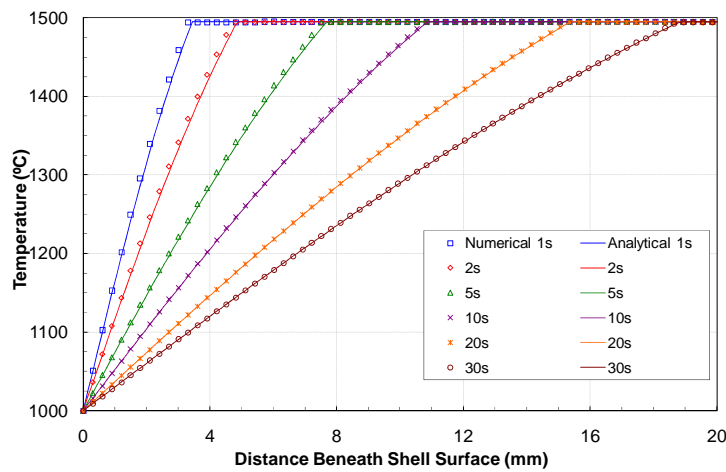


Figure 3. Temperatures through solidifying plate at different times comparing analytical solution and numerical predictions.

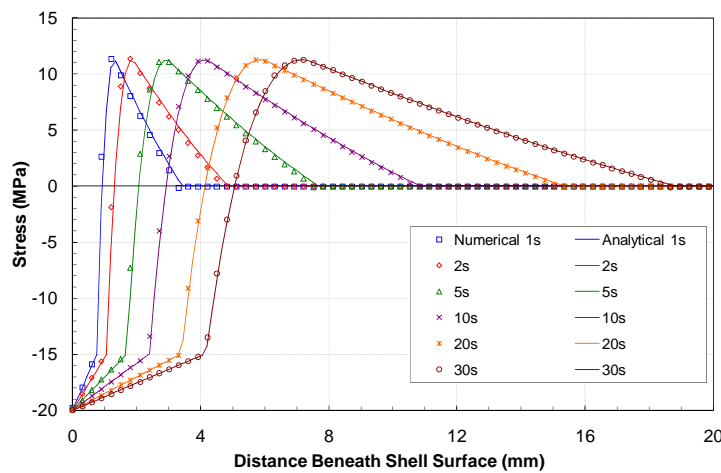


Figure 4. Transverse (Y and Z) stress through solidifying plate at different times comparing analytical solution and numerical predictions.

6 Example Applications

6.1 Sand Casting of Braking disks

The finite element software THERCAST for thermomechanical analysis of solidification^[34] has been used in the automotive industry to predict distortion of grey-iron braking discs cast in sand molds.^[60] Particular attention has been paid to the interaction between the deformation of internal sand cores and the cast parts. This demands a global coupled thermomechanical simulation, as presented above. Figure 5 illustrates the discretization of the different domains involved in the calculation. The actual cooling scenario has been simulated: cooling in mold for 45 min, shake out and air cooling for 15 min. Figure 6 shows the temperature evolution at different points in a horizontal cross section at mid-height in the disc, revealing: solidification after 2 min, and solid state phase change after 20 min. The calculated deformation of the core

blades shows thermal buckling due to the very high temperature, and constraint of their dilatation, as shown in Figure 7. This deformation causes a difference in thickness between the two braking tracks of the disc. Such a defect needs heavy and costly machining operations to produce quality parts. Instead, process simulation allows the manufacturer to test alternative geometries and process conditions in order to minimize the defect.

Similar thermomechanical calculations have been made for plain discs, leading to comparisons with residual stress measurements by means of neutrons and X-ray diffraction.^[61] As shown in Figure 8, calculations are consistent with measurements to within 10 MPa.



Figure 5. Finite element meshes of the different domains: part, core, and two half molds.

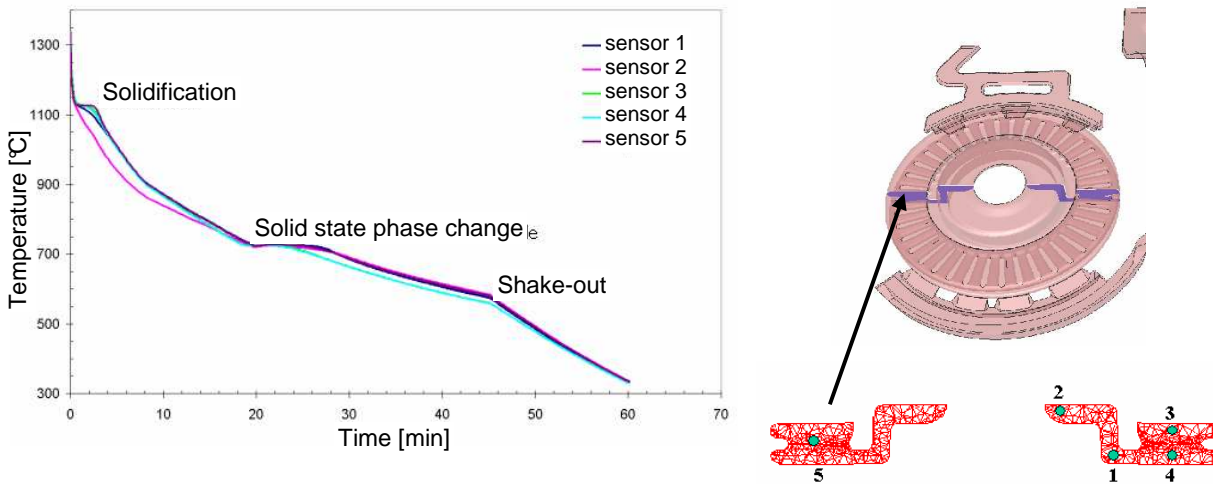


Figure 6. Temperature evolution in the part at different points located in the indicated section.

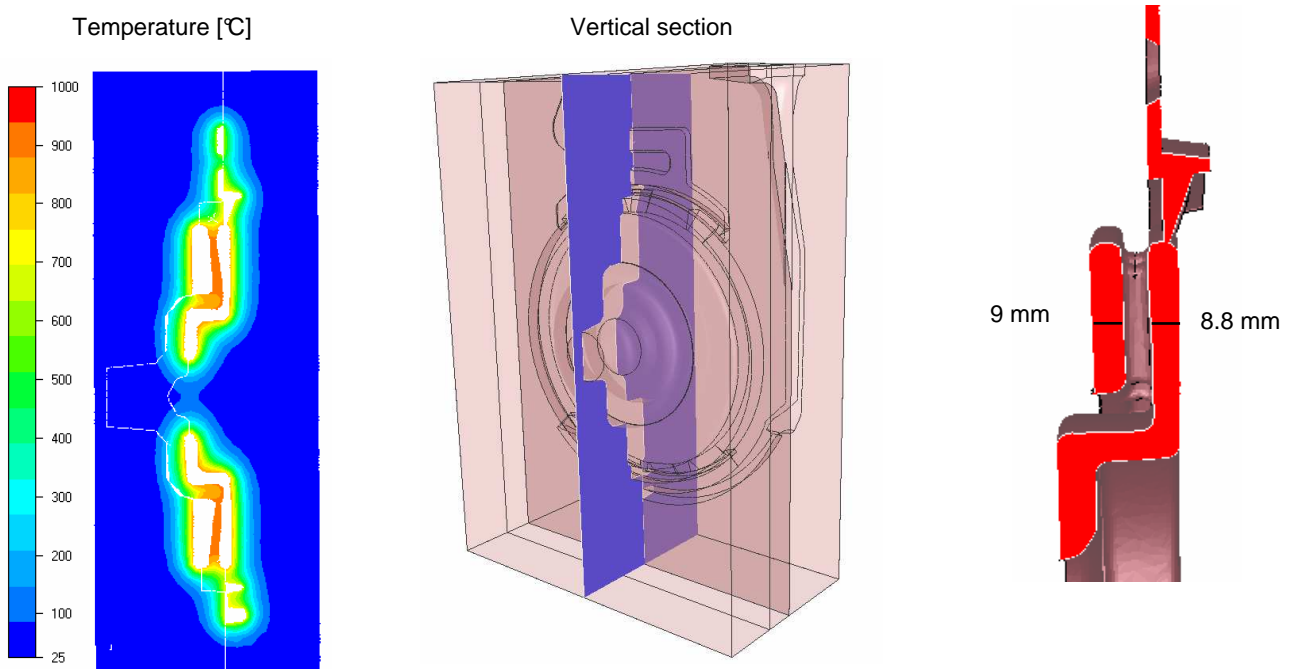


Figure 7. Deformation of core blades in a radial section, after a few seconds of cooling. On the left, displacements are magnified ($\times 100$). The temperature distribution is superimposed. On the right, the difference in thickness between the two braking tracks is shown.

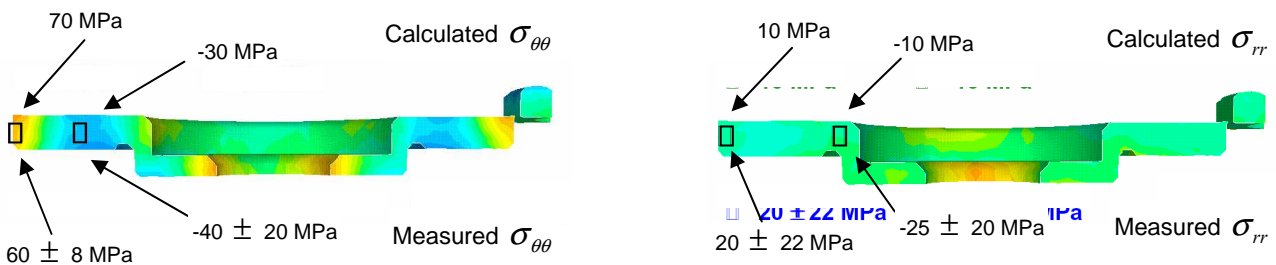


Figure 8. Residual hoop stresses (left) and radial stresses (right) in a radial section on as-cast plain discs made of grey iron. Top line: calculated values; bottom line: measured values.

6.2 Continuous Casting of Steel Slabs

Thermomechanical simulations are used by steelmakers to analyze stresses and strains both in the mold and in the secondary cooling zone below. One goal is to quantify the bulging of the solidified crust between the supporting rolls which is responsible for the tensile stress state in the mushy core, which in turn induces internal cracks and macrosegregation^[62, 63] Two and three-dimensional finite element models have been recently developed, for the entire length of the caster using THERCAST, as described elsewhere.^[40, 64] The constitutive models were presented in section 2. Contact with supporting rolls is simulated with the penalty formulation discussed in section 4.2, adapting penalty coefficients for the different rolls continuously to control numerical penetration of the strand.

Figure 9 shows results for a vertical-curved machine (strand thickness 0.22 m, casting speed 0.9 m/min, material Fe-0.06wt%C) at around 11 m below the meniscus. The pressure distribution reveals a double alternation of compressive and depressive zones. First, the strand surface is in a compressive state under the rolls where the pressure reaches its maximum, 36 MPa. Conversely, it is in a depressive (tensile) state between rolls, where the pressure is minimum (-9 MPa). Near the solidification front (i.e. close to the solidus isotherm), the stress alternates between tension (negative pressure of about -2 MPa) beneath the rolls, and compression in between, (2 to 3 MPa). These results agree with previous structural analyses of the deformation of the solidified shell between rolls, such as those carried out in static conditions by Wünnenberg,^[65] Miyazawa and Schwerdtfeger^[62] or by Kajitani et al.^[66] on small slab sections moving downstream between rolls and submitted to the metallurgical pressure onto the solidification front.

The influence of process parameters on the thermomechanical state of the strand can then be studied using such numerical models. An example is given in Figure 10, presenting the sensitivity of bulging to the casting speed. It can also be seen that bulging predictions are sensitive to the roll pitch, a larger pitch between two sets of rolls inducing an increased bulging. These numerical simulations can then be used to study possible modifications in the design of continuous casters, such as the replacement of large rolls by smaller ones in order to reduce the pitch and the associated bulging.^[67]

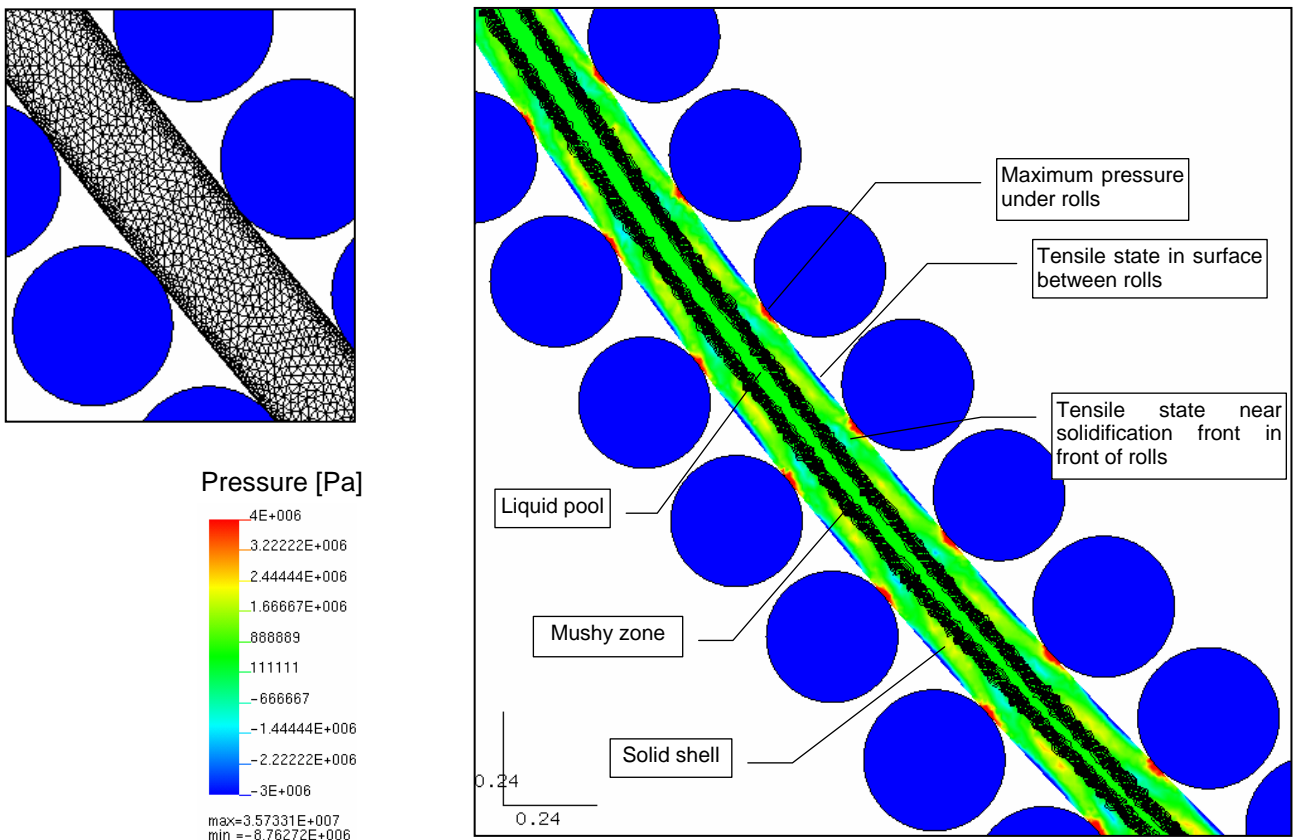


Figure 9. Predictions in the middle of the secondary cooling zone, about 11 m below the meniscus. The finite element mesh, (top left) features a fine band of 20 mm. The pressure distribution (right) reveals alternating stress, including tension near the solidification front (the mushy zone is materialized by 20 lines separated by an interval $\Delta g_i = 0.05$).

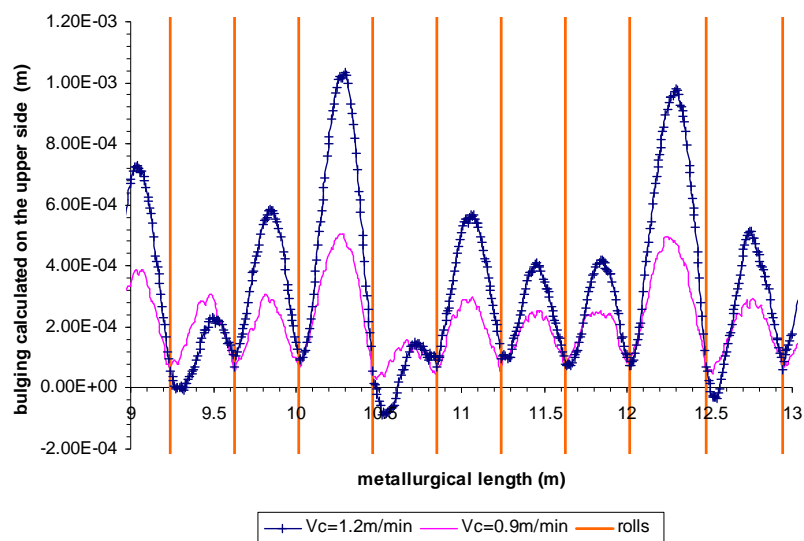


Figure 10. Slab bulging calculated at two different casting speeds: 0.9 m/min and 1.2 m/min. The slab bulging increases with the casting speed.^[67]

7 Hot tearing analysis

Hot tear crack formation is one of the most important consequences of stress during solidification. Hot tearing is caused by a combination of tensile stress and metallurgical embrittlement. It occurs at temperatures near the solidus when strain concentrates within the interdendritic liquid films, causing separation of the dendrites and intergranular cracks at very small strains (on the order of 1 percent). This complex phenomenon depends on the ability of liquid to flow through the dendritic structure to feed the volumetric shrinkage, the strength of the surrounding dendritic skeleton, the grain size and shape, the nucleation of supersaturated gas into pores or crack surfaces, the segregation of solute impurities, and the formation of interfering solid precipitates. The subsequent refilling of hot tears with segregated liquid alloy can cause internal defects that are just as serious as exposed surface cracks. The hot tearing of aluminum alloys is reviewed elsewhere.^[68] Hot tearing phenomena are too complex, too small-scale, and insufficiently understood to model in detail, so several different criteria have been developed to predict hot tears from the results of a thermal-mechanical analysis.

7.1 Thermal-analysis Criteria

Casting conditions that produce faster solidification and alloys with wider freezing ranges are more prone to hot tears. Thus, many criteria are solely based on thermal analysis. One^[69] simply compares the local time spent between two critical solid fractions g_{s1} and g_{s2} (typically 0.9 and 0.99, respectively), with the total local solidification time (or a reference solidification time). The “hot cracking susceptibility” is defined as:

$$HCS_{Clyme} = \frac{t_{0.99} - t_{0.90}}{t_{0.90} - t_{0.40}} \quad (27)$$

7.2 Classical mechanics criteria

Criteria based on classical mechanics often assume cracks will form when a critical stress is exceeded, and they are popular for predicting cracks at lower temperatures^[70-73]. This critical stress depends greatly on the local temperature and strain rate. Its accuracy relies on measurements, such as the submerged split-chill tensile test for hot tearing.^[74-76]

Measurements often correlate hot tear formation with the accumulation of a critical level of mechanical strain while applying tensile loading within a critical solid fraction where liquid feeding is difficult. This has formed the basis for many hot-tearing criteria. That of Yamanaka et al.^[77] accumulates inelastic deformation over a brittleness temperature range, which is defined, for example as $g_s \in [0.85, 0.99]$ for a Fe-0.15wt%C steel grade. The local condition for fracture initiation is then:

$$\sum_{g_{s1}}^{g_{s2}} \Delta \epsilon^{in} \geq \epsilon_{cr} \quad (28)$$

in which the critical strain ϵ_{cr} is 1.6% at a typical strain rate of $3 \times 10^{-4} \text{ s}^{-1}$. Careful measurements during bending of solidifying steel ingots have revealed critical strains ranging from 1 to 3.8%.^[77, 78] The lowest values were found at high strain rate and in crack-sensitive grades (e.g. high-sulfur peritectic steel).^[77] In aluminum rich Al-Cu alloys, critical strains were reported from 0.09 to 1.6% and were relatively independent of strain rate.^[79] Tensile stress is also a requirement for hot tear formation.^[77] The maximum tensile stress occurs just before formation of a critical flaw.^[79]

The critical strain decreases with increasing strain rate, presumably because less time is available for liquid feeding, and also decreases for alloys with wider freezing ranges. Won et al.^[80] suggested the following empirical equation for the critical strain in steel, based on fitting measurements from many bend tests:

$$\epsilon_{cr} = \frac{0.02821}{\dot{\epsilon}^{0.3131} \Delta T_B^{0.8638}} \quad (29)$$

where $\dot{\epsilon}$ is the strain rate and ΔT_B is the brittle temperature range, defined between the temperatures corresponding to solid fractions of 0.9 and 0.99.

7.3 Mechanistically-based criteria

More mechanistically-based hot-tearing criteria include more of the local physical phenomena that give rise to hot tears. Feurer,^[81] and more recently Rappaz et al.^[82] have proposed that hot tears form when the local interdendritic liquid feeding rate is not sufficient to balance the rate of tensile strain increase across the mushy zone. The criterion of Rappaz et al. predicts fracture when the strain rate exceeds a limit value that allows pore cavitation to separate the residual liquid film between the dendrites:

$$\dot{\epsilon} \geq \frac{1}{R} \left[\frac{\lambda_2^2 \|\nabla T\| \rho_L}{180 \mu_l \rho_s} (p_m - p_c) - v_T \frac{\rho_s - \rho_L}{\rho_s} H \right] \quad (30)$$

in which μ_l is the dynamic viscosity of the liquid phase, λ_2 is the secondary dendrite arm spacing, p_m is the local pressure in the liquid ahead of the mushy zone, p_c is the cavitation pressure, v_T is the velocity of the solidification front. The quantities R and H depend on the solidification path of the alloy:

$$R = \int_{T_2}^{T_1} \frac{g_s^2 F(T)}{g_l^3} dT \quad H = \int_{T_2}^{T_1} \frac{g_s^2}{g_l^2} dT \quad F(T) = \frac{1}{\|\nabla T\|} \int_{T_2}^T g_s dT \quad (31)$$

where the integration limits are calibration parameters which also have physical meaning.^[83] The upper limit T_1 may be the liquidus or the coherency temperature, while the lower limit T_2 typically is within the solid fraction range of 0.95-0.99.^[84]

7.4 Case Study: Billet Casting Speed Optimization

A Lagrangian model of temperature, distortion, strain, stress, hot tearing has been applied to predict the maximum speed for continuous-casting of steel billets without forming off-corner internal cracks. The two-dimensional transient finite-element thermal-mechanical model, CON2D^[20, 21] has been used to track a transverse slice through the solidifying steel strand as it moves downwards at the casting speed to reveal the entire 3-D stress state. The 2-D assumption produces reasonable temperature predictions because axial (z-direction) conduction is negligible relative to axial advection.^[50] In-plane mechanical predictions are also reasonable because bulging effects are small and the undiscretized casting direction is modeled with the appropriate condition of generalized plain strain. Other applications with this model include the prediction of ideal taper of the mold walls,^[85] and quantifying the effect of steel grade on oscillation mark severity during level fluctuations^[86].

The model domain is an L-shaped region of a 2-D transverse section, shown in Figure 11. Removing the central liquid region saves computation and lessens stability problems related to element “locking”.

Physically, this “trick” is important in two-dimensional domains because it allows the liquid volume to change without generating stress, which mimics the effect of fluid flow into and out of the domain that occurs in the actual open-topped casting process. Simulations start at the meniscus, 100 mm below the mold top, and extend through the 800-mm long mold and below, for a caster with no sub-mould support. The instantaneous heat flux, given in Eq. (32), was based on plant measurements.^[45] It was assumed to be uniform around the perimeter of the billet surface in order to simulate ideal taper and perfect contact between the shell and mold. Below the mold, the billet surface temperature was kept constant at its circumferential profile at mold exit. This eliminates the effect of spray cooling practice imperfections on sub-mold reheating or cooling and the associated complication for the stress/strain development. A typical plain carbon steel was studied (0.27%*c*, 1.52%Mn, 0.34%Si) with 1500.7 °C liquidus temperature, and 1411.8 °C solidus temperature. Constitutive equation and properties are given in Sections 2.4 and 2.6.

$$q(MW/m^2) = \begin{cases} 5 - 0.2444t(\text{sec.}) & t \leq 1.0 \text{ sec.} \\ 4.7556t(\text{sec.})^{-0.504} & t > 1.0 \text{ sec.} \end{cases} \quad (32)$$

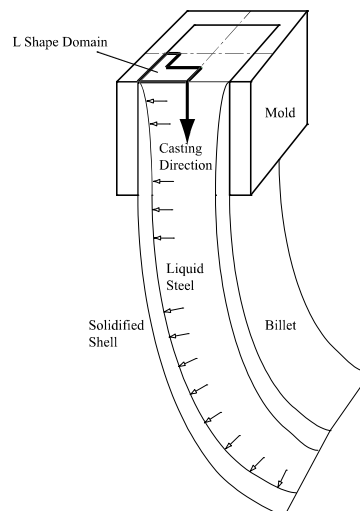


Figure 11. Model domain.

Sample results are presented here for one-quarter of a 120 mm square billet cast at speeds of 2.0 and 5.0 m/min. The latter is the critical speed at which hot-tear crack failure of the shell is just predicted to occur. The temperature and axial (*z*) stress distributions in a typical section through the wideface of the steel shell cast at 2.0 m/min are shown in Figure 12 and Figure 13 at four different times during cooling in the mold. Unlike the analytical solution in Figure 3, the surface temperature drops as time progresses. The corresponding stress distributions are qualitatively similar to the analytical solution (Figure 4). The stresses increase with time, however, as solidification progresses. The realistic constitutive equations produce a large region of tension near the solidification front. The magnitude of these stresses (and the corresponding strains) are not predicted to be enough to cause hot tearing in the mold, however. The results from two different codes reasonably match, demonstrating that the formulations are accurately implemented, convergence has been achieved, and that the mesh and time-step refinement are sufficient.

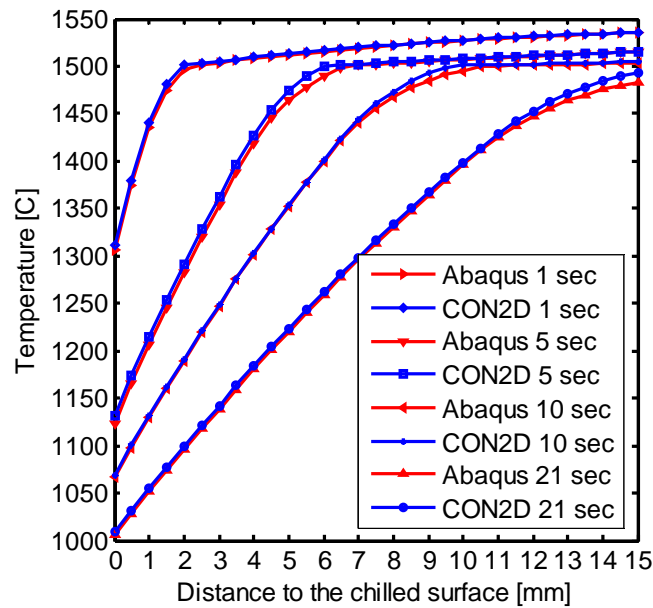


Figure 12. Temperature distribution along the solidifying slice in continuous casting mold.

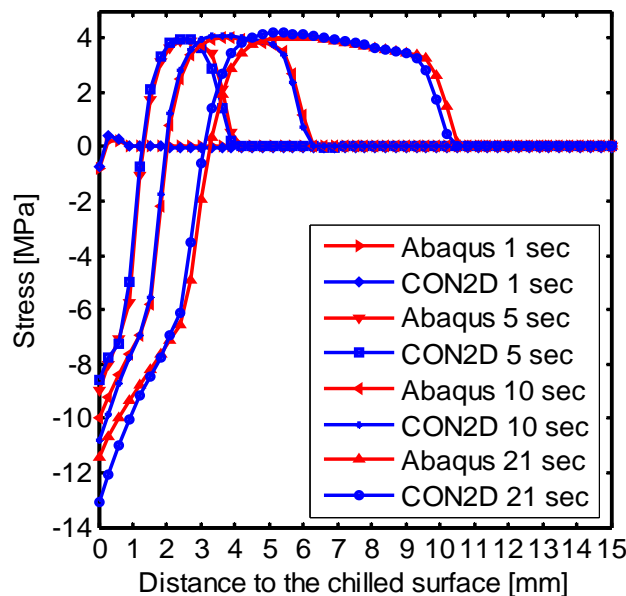


Figure 13. Lateral (y and z) stress distribution along the solidifying slice in continuous casting mold.

Figure 14(a) shows the distorted temperature contours near the strand corner at 200 mm below the mold exit, for a casting speed of 5.0 m/min. The corner region is coldest, owing to two-dimensional cooling. The shell becomes hotter and thinner with increasing casting speed, owing to less time in the mold. This weakens the shell, allowing it to bulge more under the ferrostatic pressure below the mold.

Figure 14(b) shows contours of “hoop” stress constructed by taking the stress component acting perpendicular to the dendrite growth direction, which simplifies to σ_x in the lower right portion of the domain and σ_y in the upper left portion. High values appear at the off-corner sub-surface region, due to a

hinging effect that the ferrostatic pressure over the entire face exerts around the corner. This bends the shell around the corner and generates high subsurface tensile stress at the weak solidification front in the off-corner subsurface location. This tensile stress peak increases slightly and moves towards the surface at higher casting speed. Stress concentration is less and the surface hoop stress is compressive at the lower casting speed. This indicates no possibility of surface cracking. However, tensile surface hoop stress is generated below the mold at high speed in Figure 14(b) at the face center due to excessive bulging. This tensile stress, and the accompanying hot-tear strain, might contribute to longitudinal cracks which penetrate the surface.

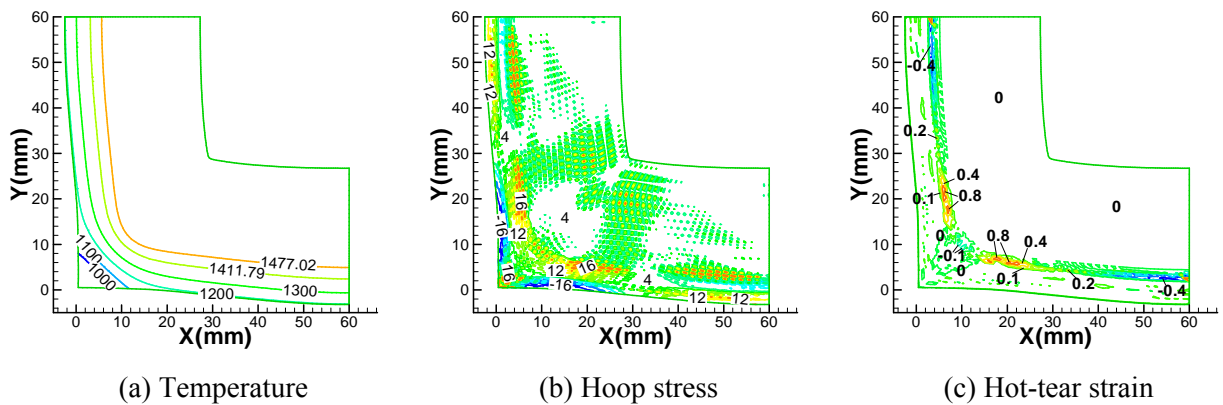


Figure 14. Distorted contours at 200 mm below mold exit.

Hot tearing was predicted using the criterion in Eq. (28) with the critical strain given in Eq. (29). Inelastic strain was accumulated for the component oriented normal to the dendrite growth direction, because that is the weakest direction and corresponds to the measurements used to obtain Eq. (29). Figure 14(c) shows contours of hot-tear strain in the hoop direction. The highest values appear at the off-corner subsurface region in the hoop direction. Moreover, significantly higher values are found at higher casting speeds. For this particular example, hot-tear strain exceeds the threshold at 12 nodes, all located near the off-corner subsurface region. This is caused by the hinging mechanism around the corner. No nodes fail at the center surface, in spite of the high tensile stress there. The predicted hot-tearing region matches the location of off-corner longitudinal cracks observed in sections through real solidifying shells, such as the one pictured in Figure 15. The bulged shape is also similar.

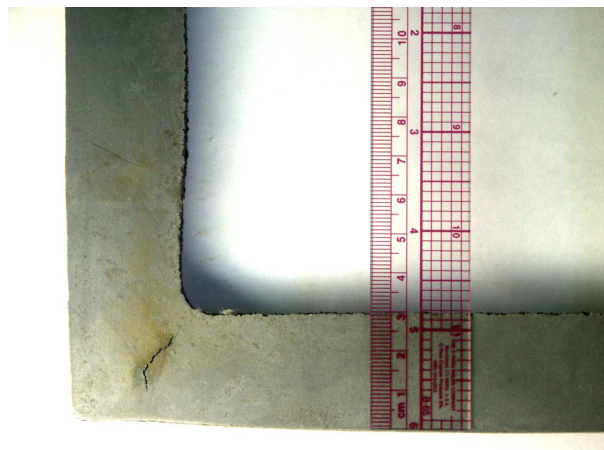


Figure 15. Off-corner internal crack in break-out shell from a 175 mm square bloom.

Results from many computations were used to find the critical speed to avoid hot tear cracks as a function of section size and working mold length, presented in Figure 16.^[46] These predictions slightly exceed plant practice, which is generally chosen by empirical trial and error. This suggests that plant conditions such as mold taper are less than ideal, that other factors limit casting speed, or those speeds in practice could be increased. The qualitative trends are the same.

This quantitative model of hot tearing provides many useful insights into the continuous casting process. Larger section sizes are more susceptible to bending around the corner, so have a lower critical speed, resulting in less productivity increase than expected. The trend towards longer molds over the past three decades enables a higher casting speed without cracks by producing a thicker, stronger shell at mold exit.

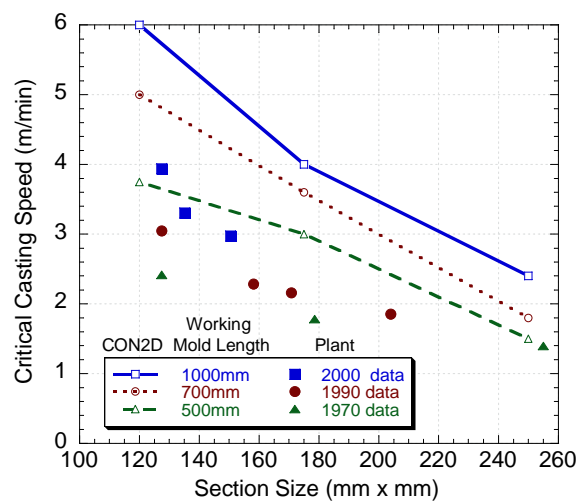


Figure 16. Comparison of critical casting speeds, based on hot-tearing criterion, and typical plant practice.^[87]

8 Conclusions

Mechanical analysis of casting processes is growing in sophistication, accuracy, and phenomena incorporated. Quantitative predictions of temperature, deformation, strain, stress, and hot tearing in real casting processes are becoming possible. Computations are still hampered by the computational speed and limits of mesh resolution, especially for realistic three-dimensional geometries and defect analysis.

Acknowledgements

The authors wish to thank the Continuous Casting Consortium and the National Center for Supercomputing Applications at the University of Illinois, the French Ministry of Industry, the French Technical Center of Casting Industries (CTIF) and the companies ArcelorMittal, Ascometal, Aubert et Duval, Industeel and PSA Peugeot-Citroën, for support of this work.

References

1. Mase, G.E. and G.T. Mase, Continuum mechanics for engineers, CRC Press Second Edition, 1999.

2. Thomas, B.G., Q. Yuan, S. Sivaramakrishnan, T. Shi, S.P. Vanka and M.B. Assar, "Comparison of Four Methods to Evaluate Fluid Velocities in a Continuous Casting Mold," ISIJ Internat., Vol. 41 (10), 2001, 1266-1276.
3. Yuan, Q., B. Zhao, S.P. Vanka and B.G. Thomas, "Study of Computational Issues in Simulation of Transient Flow in Continuous Casting," Steel Research International, Vol. 76 (1, Special Issue: Simulation of Fluid Flow in Metallurgy), 2005, 33-43.
4. Yuan, Q., S. Sivaramakrishnan, S.P. Vanka and B.G. Thomas, "Computational and Experimental Study of Turbulent Flow in a 0.4-Scale Water Model of a Continuous Steel Caster," Metall. & Mater. Trans., Vol. 35B (5), 2004, 967-982.
5. Beckermann, C., "Macrosegregation," in Encyclopedia of Materials: Science and Technology, Elsevier, 2001, 4733-4739.
6. Lesoult, G., C.-A. Gandin and N.T. Niane, "Segregation during solidification with spongy deformation of the mushy zone," Acta Materiali, Vol. 51, 2003, 5263-5283.
7. L.C. Nicolli, A. Mo and M. M'Hamdi, "Modeling of macrosegregation caused by volumetric deformation in a coherent mushy zone," Metall. Mater. Trans. A, Vol. 36, 2005, 433-442.
8. V.D. Fachinotti, S. Le Corre, N. Triolet, M. Bobadilla and M. Bellet, "Two-phase thermo-mechanical and macrosegregation modelling of binary alloys solidification with emphasis on the secondary cooling stage of steel slab continuous casting," Int. J. Num. Meth. Eng., 2006, in press.
9. Ludwig, O., C.-L. Martin, J.-M. Drezet and M. Suéry, "Rheological behaviour of Al-Cu alloys during solidification: constitutive modelling, experimental identification and numerical study," Met. Mat. Trans., Vol. 36A, 2005, 1525-1535.
10. Estrin, Y., "A versatile unified constitutive model based on dislocation density evolution," in Constitutive modelling – Theory and Application, Vol. MD-vol26 / AMD-vol121, ASME, New York 1991, 65-75.
11. C. Agelet de Saracibar, M. Cervera and M. Chiumenti, " On the constitutive modeling of coupled thermomechanical phase-change problems," Int. J. Plasticity, Vol. 17, 2001, 1565-1622.
12. Sengupta, J., S.L. Cockcroft, D.M. Maijer and A. Larouche, "Quantification of temperature, stress, and strain fields during the start-up phase of direct chill casting process by using a 3D fully coupled thermal and stress model for AA5182 ingots," Materials Science and Engineering A, Vol. 397, 2005, 157-177.
13. Kelly, J.E., K.P. Michalek, T.G. O'Connor, B.G. Thomas and J.A. Dantzig, "Initial Development of Thermal and Stress Fields in Continuously Cast Steel Billets," Metall. Trans. A, Vol. 19A (10), 1988, 2589-2602.
14. Huespe, A.E., A. Cardona and V. Fachinotti, "Thermomechanical model of a continuous casting process," Computer Methods in Appl. Mech. & Engr., Vol. 182 (3), 2000, 439-455.
15. MARC Users Manual, MARC Analysis Research Corp., Palo Alto, CA, 1991.
16. "ABAQUS Theory Manual v6.0," Abaqus, Inc., Pawtucket, Rhode Island, 2004.
17. Hakonsen, A. and D. Mortensen, Modeling of Casting, Welding and Advanced Solidification Processes VII,), The Minerals, Metals and Materials Society, Warrendale, USA, 1995, 963-970.
18. Fjaer, H.G. and A. Mo, "ALSPEN - A mathematical model for thermal stresses in DC-cast Al billets," Metall. Trans., Vol. 21B (6), 1990, 1049-1061.
19. G. Laschet, J. Jakumeit and S. Benke, "Thermo-mechanical analysis of cast/mould interaction in casting processes, ," Z. Metallkd., Vol. 95, 2004, 1087-1096.
20. Li, C. and B.G. Thomas, "Thermo-Mechanical Finite-Element Model of Shell Behavior in Continuous Casting of Steel," Metal. & Material Trans. B., Vol. 35B (6), 2004, 1151-172.
21. Koric, S. and B.G. Thomas, "Efficient Thermo-Mechanical Model for Solidification Processes," Int. J. Num. Meths. Eng., Vol. 66 (12), 2006, 1955-1989.

22. MAGMASOFT. <http://www.magmaflow.com>. (2007),
23. PROCAST. Procast, http://www.esi-group.com/SimulationSoftware/Die_Casting_Solution/Products/Casting_simulation/. (2007),
24. M. Samonds and J.Z. Zhu, "Coupled thermal-fluid-stress analysis of castings," Proc. MCWASP IX, 9th Int. Conf. on Modeling of Casting, Welding and Advanced Solidification Processes, P.R. Sahm, P.N. Hansen and J.G. Conley, eds., (Aachen (Germany), August 20-25, 2000), Shaker Verlag, Aachen, 2000, 80-87.
25. Drezet, J.M., A. Bughardt, H.G. Fjaer and B. Magnin, "Thermomechanical Effects in D.C. Casting of Aluminum Alloy: A Numerical Benchmark Study," Materials Science Forum 2000, Vol. 329-330, 2000, 493-500.
26. Fjaer, H.G. and A. Hakonsen, "The Mechanism of Pull-in during DC-Casting of Aluminum Sheet Ingots," Light Metals 1997, The Minerals, Metals & Materials Society, Warrendale, USA, 1997, 683-690.
27. Mo, A., M. Rappaz and L.L. Martin, Aluminum, Vol. 78 (10), 2002, 856-864.
28. J.M. Drezet, A. Bughardt, H.G. Fjaer and B. Magnin, Materials Science Forum 2000, Vol. 329-330, 2000, 493-500.
29. Henry, A., Light Metal Age, Vol. 58 (7-8), 2000, 66-67.
30. Bellet, M., O. Jaouen and I. Poitault, "An ALE-FEM approach to the thermomechanics of solidification processes with application to the prediction of pipe shrinkage," Int. J. Num. Meth. Heat Fluid Flow, Vol. 15, 2005, 120-142.
31. Zienkiewicz, O.C. and R.L. Taylor, The Finite Element Method, fourth ed., McGraw Hill, New York, NY, 1988.
32. J.-M. Drezet, B. Commet, H.G. Fjaer and B. Magnin, "Stress-strain computations of the DC casting process of aluminum alloy: a sensitivity study on material properties," Proc. MCWASP IX, 9th Int. Conf. on Modeling of Casting, Welding and Advanced Solidification Processes, P.R. Sahm, P.N. Hansen and J.G. Conley, eds., (Aachen (Germany), August 20-25, 2000), Shaker Verlag, Aachen, 2000, 33-40.
33. M. Bellet and V.D. Fachinotti, "ALE method for solidification modelling," Comput. Methods Appl. Mech. and Engrg., Vol. 193, 2004, 4355-4381.
34. Theracast. presentation. www.transvalor.com and www.sconconsultants.com. (2007),
35. Chiumenti, M., M. Cervera and C.A.d. Saracibar, "Coupled thermomechanical simulation of solidification and cooling phases in casting processes," in Proc. MCWASP XI, 11th Int. Conf. on Modeling of Casting, Welding and Advanced Solidification Processes, C.-A. Gandin and M. Bellet, eds., The Minerals, Metals & Materials Society, Warrendale, Pennsylvania, USA, 2006, 201-208.
36. Kozlowski, P., B.G. Thomas, J. Azzi and H. Wang, "Simple Constitutive Equations for Steel at High Temperature," Metall. Trans. A, Vol. 23A (3), 1992, 903-918.
37. Wray, P.J., "Plastic Deformation of Delta-Ferritic Iron at Intermediate Strain Rates," Metall. Trans. A, Vol. 7A (Nov.), 1976, 1621-1627.
38. Wray, P.J., "Effect of Carbon Content on the Plastic Flow of Plain Carbon Steels at Elevated Temperatures," Metall. Trans. A, Vol. 13A (1), 1982, 125-134.
39. Suzuki, T., K.H. Tacke, K. Wunnenberg and K. Schwerdtfeger, "Creep Properties of Steel at Continuous Casting Temperatures," Ironmaking Steelmaking, Vol. 15 (2), 1988, 90-100.
40. F. Costes, A. Heinrich and M. Bellet, "3D thermomechanical simulation of the secondary cooling zone of steel continuous casting," in Proc. MCWASP X, 10th Int. Conf. on Modeling of Casting, Welding and Advanced Solidification Processes, D.M. Stefanescu, J.A. Warren, M.R.J. & M.J.M. Krane, eds., The Minerals, Metals & Materials Society, Warrendale, Pennsylvania, USA, 2003, 393-400.

41. Donsbach, D.L. and M.W. Moyer, "Ultrasonic Measurement of Elastic Constants at Temperatures from 20 to 1100 oC," in Ultrasonic Materials Characterization, Special Pub. 596, H. Berger and M. Linzer, eds., Nat. Bureau of Standards, 1980.
42. Puhlinger, O.M., "Strand Mechanics for Continuous Slab Casting Plants," Stahl Eisen, Vol. 96 (6), 1976, 279-284.
43. Hub, D.R., "Measurement of Velocity and Attenuation of Sound in Iron up to the Melting Point," Proc. IVth Intern. Vong. Acoustics, (Copenhagen), 1962, paper 551, paper #551.
44. Mizukami, H., K. Murakami and Y. Miyashita, "Mechanical Properties of Continuously Cast Steels at High Temperatures," Tetsu-to-Hagane, Vol. 63 (146), 1977, S 652.
45. Li, C. and B.G. Thomas, "Maximum Casting Speed for Continuous Cast Steel Billets Based on Sub-Mold Bulging Computation," in Steelmaking Conf. Proc., Vol. 85, ISS, Warrendale, PA, (Nashville, TN, March 10-13, 2002), 2002, 109-130.
46. Li, C. and B.G. Thomas, "Thermo-Mechanical Finite Element Model of Bulging and Hot Tearing During Continuous Casting of Steel Billets," in Modeling of Casting, Welding, and Advanced Solidification Processes, Vol. X, D. Stefanescu, J. Warren, M. Jolly and M. Krane, eds., TMS, Warrendale, PA, (San Destin, FL, May 25-30, 2003), 2003, 385-392.
47. Harste, K., A. Jablonka and K. Schwerdtfeger, "Shrinkage and Formation of Mechanical Stresses during Solidification of Round Steel Strands," 4th Int. Conf. on Continuous Casting, (Centres de Recherches Metallurgiques and Verein Deutscher Eisenhüttenleute), Stahl und Eisen, Brussels, 1988, 633-644.
48. Harste, K., "Investigation of the shrinkage and the origin of mechanical tension during the solidification and successive cooling of cylindrical bars of Fe-C alloys," PhD Dissertation Thesis, Technical University of Clausthal, 1989, not labelled.
49. Jimbo, I. and A. Cramb, "The density of liquid iron-carbon alloys," Metall. Trans. B, Vol. 24B, 1993, 5-10.
50. Meng, Y. and B.G. Thomas, "Heat Transfer and Solidification Model of Continuous Slab Casting: CONID," Metal. & Material Trans., Vol. 34B (5), 2003, 685-705.
51. C.V. Madhusudana and L.S. Fletcher, "Contact Heat Transfer – The last decade, ," AIAA Journal, Vol. 24, 1985, 510-523.
52. M. Rappaz, M. Bellet and M. Deville, "Numerical Modeling in Materials Science and Engineering," in Springer Series in Computational Mathematics, Springer-Verlag, Berlin, 2003.
53. Nemat-Nasser, S. and Y.F. Li, "An explicit Algorithm for large-strain, large-strain rate elastic-viscoplasticity," Comp. Meths. Appl. Mech. Engng, Vol. 48, 1992, 205-219.
54. Lush, A.M., G. Weber and L. Anand, "An Implicit Time-integration Procedure for A Set of Internal Variable Constitutive Equations for Isotropic Elastic-Viscoplasticity," Int. J. Plasticity, Vol. 5, 1989, 521-549.
55. Zhu, H., "Coupled thermal-mechanical finite-element model with application to initial solidification," Thesis, University of Illinois, 1993.
56. Glowinski, R. and P.L. Talle, "Augmented Lagrangian and Operator-Splitting Methods in Non-linear Mechanics, Studies in Applied Mathematics," SIAM, Vol. 9, 1989, 295p.
57. P. Wriggers and G. Zavarise, "On contact between three-dimensional beams unergoing large deflections, ," Comm. Num. Meth. Eng., Vol. 13, 1997, 429-438.
58. O. Jaouen and M. Bellet, "A numerical mechanical coupling algorithm for deformable bodies: application to part/mold interaction in casting process," in Proc. 8th Int. Conf. on Modelling of Casting, Welding and Advanced Solidification Processes, B.G. Thomas and C. Beckermann, eds., The Minerals Metals and Materials Society, Warrendale, PA, (San Diego (CA, USA), June 7-12, 1998), 1998, 739-746.

59. Weiner, J.H. and B.A. Boley, "Elasto-plastic thermal stresses in a solidifying body," J. Mech. Phys. Solids, Vol. 11, 1963, 145-154.
60. Bellet, M., C. Aliaga and O. Jaouen, "Finite elements for a thermomechanical analysis of solidification processes," in Modeling of Casting, Welding, and Advanced Solidification Processes IX, Shaker Verlag GmbH, Aachen, 2000, 10-17.
61. David, S. and P. Auburtin, "Numerical simulation of casting processes. Benefits of thermomechanical simulation in automotive industry," in Conference Matériaux 2002, Tours, France, Proc., Vol. on CD, in French, Université Technologique de Belfort-Montbéliard, 2002, 5.
62. Miyazawa, K. and K. Schwerdtfeger, "Macro-segregation in continuously cast steel slabs: preliminary theoretical investigation on the effect of steady state bulging," Arch. Eisenhütten, Vol. 52 (11), 1981, 415-422.
63. Lesoult, G. and S. Sella, "Analysis and prevention of centreline segregation during continuous casting of steel related to deformation of the solid phase," Solid State Phenomena, Vol. 3, 1988, 167-178.
64. M. Bellet and A. Heinrich, "A two-dimensional finite element thermomechanical approach to a global stress-strain analysis of steel continuous casting," ISIJ International Vol. 44, 2004, 1686-1695.
65. Wunnenberg, K. and D. Huchingen, "Strand bulging between supporting rollers during continuous slab casting," Stahl und Eisen, Vol. 98 (6), 1978, 254-259.
66. Kajitani, T., J.-M. Drezet and M. Rappaz, "Numerical simulation of deformation-induced segregation in continuous casting of steel," Metall. Mater. Trans. A, Vol. 32, 2001, 1479-1491.
67. N. Triolet and M. Bobadilla, "Mastering steel slab internal soundness and surface quality issues through thermomechanical modelling of continuous casting," in Proc. MCWASP-XI, 11th Int. Conf. on Modelling of Casting, Welding, and Advanced Solidification Processes, C.A. Gandin and M. Bellet, eds., The Minerals, Metals and Materials Society, Warrendale, PA, (Opio, France, May 28 – June 2, 2006), 2006, 753-760.
68. D.G. Eskin, Suyitno and L. Katgerman, "Mechanical properties in the semi-solid state and hot tearing of aluminum alloys," Prog. Mat. Sci., Vol. 49, 2004, 629-711.
69. Clyne, T.W. and G.J. Davies, "Comparison between experimental data and theoretical predictions relating to dependence of solidification cracking on composition," in Solidification and Casting of Metals, The Metals Society, London, 1979, 275-278.
70. Kinoshita, K., T. Emi and M. Kasai, "Thermal Elasto-plastic Stress Analysis of Solidifying Shell in Continuous Casting Mold," Tetsu-to-Hagane, Vol. 65 (14), 1979, 2022-2031.
71. Kristiansson, J.O., "Thermal stresses in the early stage of solidification of steel," J. Thermal Stresses, Vol. 5, 1982, 315-330.
72. Thomas, B.G., I.V. Samarasekera and J.K. Brimacombe, "Mathematical Model of the Thermal Processing of Steel Ingots, Part II: Stress Model," Metall. Trans. B, Vol. 18B (1), 1987, 131-147.
73. Okamura, K. and H. Kawashima, "Calculation of Bulging Strain and its Application to Prediction of Internal Cracks in Continuously Cast Slabs," in Proc. Int. Conf. Comp. Ass. Mat. Design Proc. Simul., ISIJ, Tokyo, 1993, 129-134.
74. Ackermann, P., W. Kurz and W. Heinemann, "In Situ Tensile Testing of Solidifying Aluminum and Al-Mg Shells," Materials Science and Engineering (75), 1985, 79-86.
75. Bernhard, C., H. Hiebert and M.M. Wolf, "Simulation of shell strength properties by the SSCT test," ISIJ International (Japan), Vol. 36 (Suppl. Science and Technology of Steelmaking), 1996, S163-S166.
76. Suzuki, M., C. Yu and T. Emi, "In-Situ Measurement of Tensile Strength of Solidifying Steel Shells to Predict Upper Limit of Casting Speed in Continuous Caster with Oscillating Mold," ISIJ International, Iron & Steel Inst. of Japan, Vol. 37 (4), 1997, 375-382.
77. Yamanaka, A., K. Nakajima, K. Yasumoto, H. Kawashima and K. Nakai, "Measurement of Critical Strain for Solidification Cracking," Modelling of Casting, Welding, and Advanced Solidification

Processes - V, M. Rappaz, M.R. Ozgu and K.W. Mahin, eds., (Davos, SW), TMS, Warrendale, PA, Vol. V, 1990, 279-284.

78. Yamanaka, A., K. Nakajima and K. Okamura, "Critical Strain for Internal Crack Formation in Continuous Casting," Ironmaking Steelmaking, Vol. 22 (6), 1995, 508-512.
79. Wisniewski, P. and H.D. Brody, "Tensile Behavior of Solidifying Aluminum Alloys," Modelling of Casting, Welding, and Advanced Solidification Processes - V, M. Rappaz, M.R. Ozgu and K.W. Mahin, eds., (Davos, SW), TMS, Warrendale, PA, Vol. V, 1990, 273-278.
80. Won, Y.-M., T.J. Yeo, D.J. Seol and K.H. Oh, "A New Criterion for Internal Crack Formation in Continuously Cast Steels," Metall. Mater. Trans. B, Vol. 31B, 2000, 779-794.
81. Feurer, U., "Mathematisches modell der Warmrissneigung von binären aluminium legierungen," Giessereiforschung Vol. 28 (75-80), 1976.
82. Rappaz, M., J.-M. Drezet and M. Gremaud, "A New Hot-Tearing Criterion," Metall. Mater. Trans. A, Vol. 30A (2), 1999, 449-455.
83. Drezet, J.M. and M. Rappaz, "Prediction of Hot Tears in DC-Cast Aluminum Billets," in Light Metals, J.L. Anjier, ed. TMS, Warrendale, PA, 2001, 887-893.
84. M. M'Hamdi, S. Benum, D. Mortensen, H.G. Fjaer and J.M. Drezet, "The importance of viscoplastic strain rate in the formation of center cracks during the start-up phase of direct-chill cast aluminium extrusion ingots," Metall. Mater. Trans. A, Vol. 34, 2003, 1941-1952.
85. Thomas, B.G. and C. Ojeda, "Ideal Taper Prediction for Slab Casting," ISSTech Steelmaking Conference, (Indianapolis, IN, USA, April 27-30, 2003), Vol. 86, 2003, 396-308.
86. Sengupta, J. and B.G. Thomas, "Effect of a Sudden Level Fluctuation on Hook Formation During Continuous Casting of Ultra-Low Carbon Steel Slabs," in Modeling of Casting, Welding, and Advanced Solidification Processes XI (MCWASP XI) Conference, M.B. C.Z. Gandin, and J.E. Allison, ed., (Opio, France, May 28-June 2, 2006), 2006, 727-236.
87. Howard, E. and D. Lorento, "Development of High Speed Casting," in 1996 Electric Furnace Conference Proceedings, ISS, Warrendale, PA, (Dallas, TX, Dec. 9-12, 1996), 1996.